Brian R. Elbing[1]
Mechanical and Aerospace Engineering,
Oklahoma State University,
Engineering North 218,
Stillwater, OK 74078
e-mail: elbing@okstate.edu

Libin Daniel[2]
Mechanical and Aerospace Engineering,
Oklahoma State University,
Stillwater, OK 74078
e-mail: Libin.Daniel@gulfstream.com

Yasaman Farsiani
Mechanical and Aerospace Engineering,
Oklahoma State University,
Engineering North 218,
Stillwater, OK 74078
e-mail: yasaman.farsiani@okstate.edu

Christopher E. Petrin
Mechanical and Aerospace Engineering,
Oklahoma State University,
Engineering North 218,
Stillwater, OK 74078
e-mail: cepetri@okstate.edu

Design and Validation of a Recirculating, High-Reynolds Number Water Tunnel

Commercial water tunnels typically generate a momentum thickness based Reynolds number (Re_θ) ∼1000, which is slightly above the laminar to turbulent transition. The current work compiles the literature on the design of high-Reynolds number facilities and uses it to design a high-Reynolds number recirculating water tunnel that spans the range between commercial water tunnels and the largest in the world. The final design has a 1.1 m long test-section with a 152 mm square cross section that can reach speed of 10 m/s, which corresponds to $Re_\theta = 15{,}000$. Flow conditioning via a tandem configuration of honeycombs and settling-chambers combined with an 8.5:1 area contraction resulted in an average test-section inlet turbulence level <0.3% and negligible mean shear in the test-section core. The developing boundary layer on the test-section walls conform to a canonical zero-pressure-gradient (ZPG) flat-plate turbulent boundary layer (TBL) with the outer variable scaled profile matching a 1/7th power-law fit, inner variable scaled velocity profiles matching the log-law and a shape factor of 1.3. [DOI: 10.1115/1.4039509]

1 Introduction

Typical commercial recirculating water tunnels achieve a momentum thickness based Reynolds number (Re_θ) on the order of 10^3, which is slightly above that required for laminar to turbulent transition. This is not ideal for studying Reynolds number dependent turbulent flow phenomena, such as velocity profile modifications from drag reducing polymer solutions [1,2] or helicopter wake structures [3]. Consequently, much of this work is performed in extremely large government owned water tunnels such as the U.S. Navy Large Cavitation Channel (LCC) [4,5] or the Garfield Thomas Water Tunnel (GTWT) [6,7]. The LCC, the world's largest water tunnel, can achieve $\mathrm{Re}_\theta \sim 10^5$, but the operation cost is extremely high. Consequently, facilities that can achieve $\mathrm{Re}_\theta \sim 10^4$ are ideal for studying Reynolds number dependent turbulent phenomena, which was the primary specification for the current facility.

There are several established facilities that fit this operation range [8–16], but they were built as part of major research programs (i.e., sufficient funds for prototype testing components) and/or refurbished facilities (i.e., key design considerations already fixed). Furthermore, the limited literature on these designs is difficult to obtain since it is typically in technical reports, conference papers, and/or theses. Thus, the current work compiles information from a wide range of facilities (see Ref. [17] for complete list), which is a guide to the overall design of a relatively low-cost water tunnel capable of achieving Reynolds numbers comparable to any nongovernment owned facility and verifies the design with characterization of the as-built tunnel performance. The completed facility (schematically shown in Fig. 1) bridges the gap between commercial water tunnels that are barely turbulent and the world's largest facilities [4–7,18–22]. The test-section specifications were (i) $\mathrm{Re}_\theta \geq 10^4$, (ii) maximize optical access, and (iii) minimize inlet flow nonuniformity. The remainder of this paper covers the design of individual components (Sec. 2), characterization of the completed facility (Sec. 3), and conclusions (Sec. 4). The interested reader is directed to the previous work [17,23,24] for more detailed discussion on structural design, fabrication, and installation.

[1]Corresponding author.

[2]Present address: Flight Test Engineering, Gulftstream Aerospace Corporation, Savannah, GA 31408.

Contributed by the Fluids Engineering Division of ASME for publication in the Journal of Fluids Engineering. Manuscript received July 2, 2017; final manuscript received February 15, 2018; published online March 29, 2018. Assoc. Editor: Elias Balaras.

2 Water Tunnel Design and Construction

2.1 Test Section. Test-section design is driven by the application, operation range, and instrumental suite (optical and mechanical access). The current facility focuses on modifications to canonical turbulent boundary layers (TBLs). The maximum length (∼1 m) was set to achieve the required rigidity, flatness, and surface smoothness without excessive costs. Momentum integral analysis with a 1/7th velocity profile on a zero-pressure-gradient (ZPG) flat-plate [25] estimates the outlet boundary layer thickness $(\delta/x = 0.16\mathrm{Re}_x^{-1/7})$ to be ≥16 mm. Here, Re_x $(= U_e x/\nu)$ is the downstream-based Reynolds number, ν is the kinematic viscosity (∼10^{-6} m^2/s), x is the downstream distance from the inlet, and U_e is the local freestream (external) speed. The TBL overlap region is unaltered from the log-law $\left(u^+ = \ln y^+/\kappa + B\right)$ when the dimensionless acceleration parameter $K' = \left(\nu/U_e^2\right)dU_e/dx < 1.62 \times 10^{-6}$ [26]. Here, $y^+(= y/l_\nu)$ is the inner variable scaled wall-normal distance, $u^+(= u/u_\tau)$ is the inner variable scaled velocity, $u_\tau(= \sqrt{\tau_w/\rho})$ is the friction velocity, $l_\nu(= \nu/u_\tau)$ is the viscous wall unit, τ_w is wall shear stress, ρ is the fluid density, κ (≈0.41) is the Kármán constant, and B (≈5.0) is the intercept constant. Accounting for displacement thickness $\left(\delta^*/x = 0.02\mathrm{Re}_x^{-1/7}\right)$, the same analysis can estimate dU_e/dx. The K' criterion is achieved with a 15 mm × 15 mm cross section, but the final size was increased (152 mm × 152 mm) because recent high-Reynolds number findings [27,28] suggest that mild pressure-gradients can alter velocity profiles.

The as-built test-section has a flange-to-flange total length of 1.1 m with a viewable length of 0.914 m (Fig. 2) on all sides except the top, which has a 114 mm × 76 mm panel to accommodate an injection plate [17]. Edge fairings were not used and the

 Copyright © 2018 by ASME

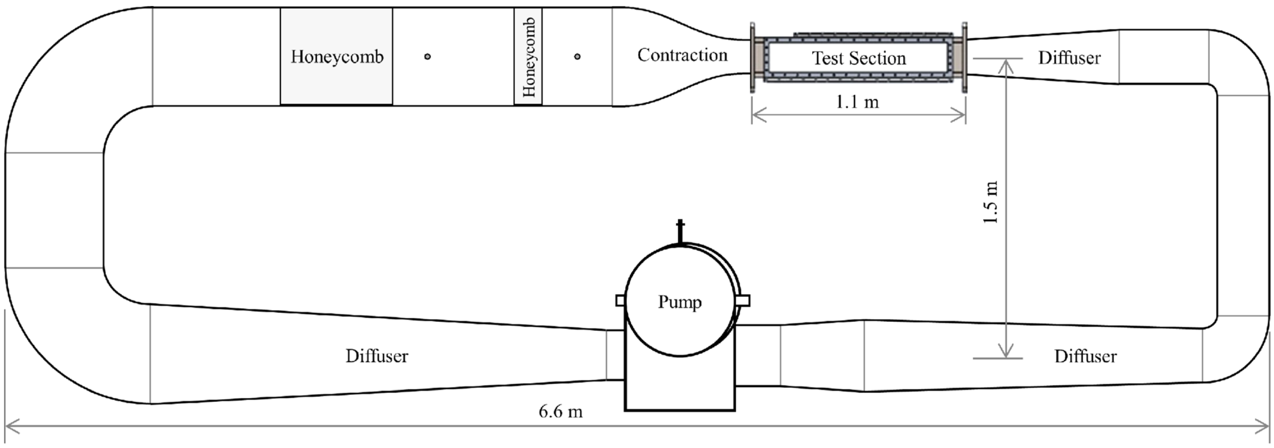

Fig. 1 Schematic of the high-Reynolds number, low turbulence recirculating water tunnel. Ports downstream of honeycomb sections are temperature and static pressure measurements.

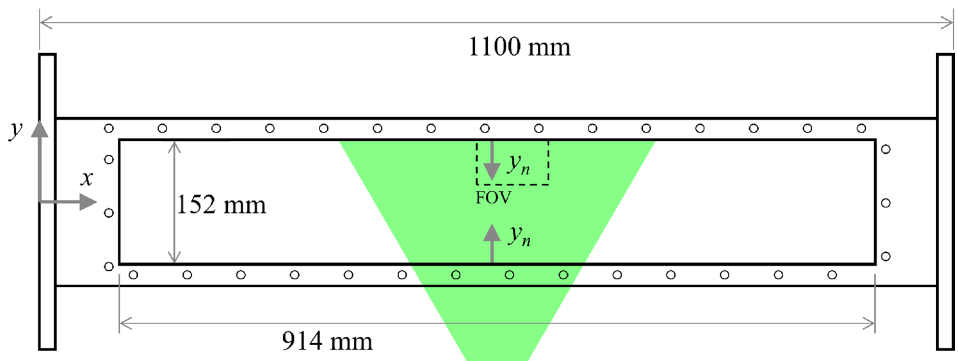

Fig. 2 Test section schematic of the particle image velocimetry (PIV) measurement orientation

frame designed to facilitate direct line-of-sight of the tunnel wall. A trip of uniformly distributed 122 μm silicon carbide grit was located around the test-section inlet perimeter. When pressurized ($p_{\max} = 276$ kPa), the acrylic walls have a maximum displacement of 115 μm [17]. The resulting local curvature has a negligible impact on the velocity profile but is nontrivial compared to l_ν. Thus, the wall location must be identified for each operating condition. The stainless steel frame has an average roughness height (R_a) of 0.8 μm. Converting R_a to Colebrook type roughness (k_c) [29,30] and noting $l_\nu \geq 2.0\,\mu$m, the maximum $k^+ = k_c/l_\nu$ is 0.6 to 1.7. This is acceptable since hydraulically smooth is $k^+ < 4$ and the majority of the TBL develops on the smoother acrylic windows.

2.2 Flow Conditioning. The ideal test-section inlet velocity would be steady and uniform with negligible turbulence. This is never realized because 90 deg elbows introduce swirl, flow-straighteners remove swirl while introducing turbulence, and boundary layers cause local flow acceleration. Consequently, no ideal flow conditioning system exists and the final components in this work are not considered optimized. In the current work, flow nonuniformity was mitigated with a tandem honeycomb/settling-chamber configuration, an 8.5:1 contraction, and gradual expansion in diffusers (Fig. 1). Design/selection of the flow conditioning components assumed that flow enters some distance upstream of the test section with a high turbulence and swirl. Swirl, which is difficult to remove, is generally done with pressure-drop via a combination of screens, baffles, and/or honeycomb. Honeycomb was selected because screens in water tunnels typically need to be tight meshed, which can foul resulting in variable tunnel performance.

A tandem honeycomb configuration was selected because turning vanes were not used and the upstream turbulence level was unknown. The honeycomb sizing used experimental turbulence reduction factors and pressure-drop coefficients for a wide range of cell length and diameters [31]. An iterative process [17,23] resulted in the selection of a 610 mm (length) by 19 mm (cell diameter) polycarbonate hexagonal honeycomb (PCFR750W24, Plascore, Zeeland, MI) followed by 152 mm (length) by 6.35 mm (diameter) stainless steel honeycomb (76 μm foil, Benecor, Wichita, KS). It is recommended that 30–40 cell diameter long settling-chambers be positioned downstream of the honeycomb to utilize viscous decay to suppress their turbulent wakes [32,33]. Thus, 594 mm (31 cell diameters) and 254 mm (40 cell diameters) long settling-chambers were placed downstream of the first and second honeycomb, respectively.

A contraction reduces the turbulence intensity (TI) while accelerating the flow. The current facility contraction (and test-section diffuser) also had a round to square shape change. An alternative design with the shape change at the pump was explored, but locally the final design was more economical. Generally, the larger the contraction ratio, the better the turbulence suppression, but a 9:1 contraction ratio provides a good compromise between turbulence suppression and economic/space constraints [34]. The closest off-the-shelf pipe had an inner diameter of 495 mm, which produces an 8.5:1 contraction ratio. Contraction profile shapes have been widely studied [35–37] for low-speed facilities, and Hasselmann et al. [37] provide an in-depth analysis. While a sixth-order polynomial is recommended for multisegment contractions, the current facility used a single piece that makes a fifth-order polynomial (Eq. (1)) appropriate. Here, X_c is the streamwise coordinate measured from the test-section inlet toward the contraction inlet, Y_c is the transverse direction from the centerline, L_c is the contraction length, and Y_o/Y_L is half the test-section/contraction inlet height, respectively. The constants were determined from the contraction ratio and setting the first and second derivatives of the inlet/outlet profile to zero. Selection of L_c is ideally done via a parametric analysis [37], but the current design leveraged the fact that seven low-turbulence water tunnels (LCC, UNH HiCaT, mini-LCC, Michigan 9 in, GTWT, PSU-ARL 12 in, and St. Anthony Falls Water Tunnel) use the same profile shape. The average $L_c/2Y_L = 1.44$ (standard deviation $= 0.33$), which corresponds to $L_c = 737$ mm for the current facility

$$\frac{Y_c - Y_o}{Y_L - Y_o} = 6\left(\frac{X_c}{L_c}\right)^5 - 15\left(\frac{X_c}{L_c}\right)^4 + 10\left(\frac{X_c}{L_c}\right)^3 \quad (1)$$

Diffusers are required to complete the loop from the minimum area at the test section through the pump and back to the contraction inlet. Increasing the area minimizes pressure losses, but the expansion half-angle should not exceed 4 deg [16,32]. Separation is likely at higher angles, which will produce unsteady flow that will propagate to the test section. The fiberglass test section diffuser follows Nedyalkov [16] to expand with the square-to-round shape change. This diffuser expanded to a 254 mm diameter over a length of 762 mm, which gives an effective half-angle of 3 deg. The other diffuser sections were located on the lower leg and fabricated from 304 stainless steel. The diffuser upstream of the pump transitioned from 254 mm to 356 mm over 1.8 m length, which gives a half-angle of 1.6 deg. The diffuser was oversized (pump inlet diameter = 305 mm) to allow a short contraction section at the pump inlet to promote uniform flow into the pump. The diffuser downstream of the pump transitions from the pump outlet (254 mm) to the flow straightener diameter (495 mm) over a length of 2.5 m, which gives a 2.8 deg half angle.

2.3 Pump Sizing. The pump supplies the pressure differential (Δp) to overcome the system losses at the desired flowrate, which requires an iterative design process. The volumetric flowrate (0.232 m^3/s) is readily available given the cross section and maximum speed (10 m/s). However, the total system losses are often severely underestimated due to nonuniform flow entering components [38] and assembly imperfections. From experience, the calculated total pressure losses (91 kPa) [23] are typically 3 to 4 times smaller than the as-built. Thus, the pump specifications were $\Delta p = 300$ kPa at 0.279 m^3/s (i.e., increased Δp and flowrate). While axial-flow pumps are preferred due to their efficiency and lack of a radial velocity, significant cost savings was possible with a centrifugal pump. Thus, a horizontal split case centrifugal pump (S10B12A-4, Patterson, Toccoa, GA) with a 112 kW (150 hp) motor (MP44G3909, Baldor, Fort Smith, AR) was selected because it (i) achieved the operating condition, (ii) had a low minimum flowrate, (iii) low cost, and (iv) compact design.

3 Tunnel Characterization

3.1 Experimental Methods. The tunnel performance was primarily assessed with PIV. An image plane was illuminated with a 532 nm Nd:YAG laser (Gemini-200, New Wave, Fremont, CA) beam formed into a sheet. Light scatter from 18 μm hollow-glass-sphere tracer particles (iM30K, 3M, Maplewood, MN) was recorded with a 2560 × 2160 pixel sCMOS camera (Imager, LaVision, Göttingen, Germany). The typical field-of-view (see Fig. 2) was nominally 49 × 41 mm and images were recorded in double-frame, double-pulse mode. The velocity vector-fields were computed using standard cross-correlation methods (DaVis8, LaVision) with a final interrogation window of 16 × 16 pixels with 50% overlap. At least 100 independent vector-field realizations were used for mean velocity profiles. The x-, y-, and z-axes are aligned with the streamwise, vertical, and horizontal (completing the right-handed system) directions, respectively. The origin was placed on the centerline at the test-section inlet, but note that this is not the boundary layer origin. Also, note that TBL measurements are presented in wall normal coordinates (y_n) as shown in Fig. 2. The displacement uncertainty was ~0.1 pixels, which corresponds to ~1% uncertainty in velocity.

Since the inlet turbulence intensity was <1%, a single-component hot-film-anemometer (HFA; MiniCTA-54T42, Dantec, Skovlunde, Denmark) with a cylindrical hot-film probe (55R15, Dantec) was used. The probe was positioned at $x = 60$mm and sampled at 500 Hz. Mean HFA signals were calibrated in situ with simultaneous PIV measurements and recorded with tunnel operation conditions (temperature, pressure, and pump frequency) via a data acquisition (DAQ) card (USB-6218-BNC, NI, Austin, TX) and commercial DAQ software (LabView15.0.1, NI). Water temperature was measured via a temperature controller (CNI3253, Omega, Norwalk, CT) with a T-Type thermocouple (TC-T-1/4NPT-U-72, Omega) located 0.92 m upstream of the contraction inlet. Tunnel static pressure was monitored with a pressure transducer (PX2300-50DI, Omega) located 76 mm upstream of the contraction inlet at the test-section centerline elevation. The pump motor frequency (f_p) was manually controlled with a variable-frequency-drive (EQ7-4150C, Teco, Round Rock, TX). Calibration between U_e at the center of the test-section and f_p ($U_e = 0.3363 f_p - 0.0106$) validates the pump selection and overall facility design with the maximum $U_e = 10.1$m/s.

3.2 Inlet Turbulence. The accuracy of the inlet TI was assessed by comparing the spectra to the classic high-Reynolds number isotropic turbulence scaling (i.e., K41 theory). The temporal single-sided power spectra $S_{uu}(\omega)$ were transformed to spatial spectra via Taylor's frozen turbulence hypothesis ($kU \approx \omega$; $S_{uu}(k) \approx U\,S_{uu}(\omega)$), where k is the wavenumber ($k = 2\pi/\lambda$), λ is the wavelength, U is the mean convection velocity, $\omega(= 2\pi f)$ is the angular frequency, and f is the temporal frequency. K41 theory suggests $S_{uu}(k)/(\nu^5\varepsilon)^{1/4} = g(k\lambda_k)$, where g is an unknown function, ε is the dissipation rate of turbulent kinetic energy per unit mass (proportional to production $\varepsilon \propto U_e^3/H_c$ with H_c the test-section height), and $\lambda_k = (\nu^3\varepsilon)^{1/4}$ is the Kolmogorov length scale. Four orders of magnitude separate the production ($H_c = 152$ mm) and dissipation ($14.5 \le \lambda_k \le 27.5\,\mu$m) length scales, which suggests that there should be a measurable inertial range ($S_{uu}(k) \propto \varepsilon^{2/3}k^{-5/3}$). Spectra for the current facility are shown in Fig. 3 with much of the data following the $k^{-5/3}$ slope.

The spectra are truncated to omit frequencies above the Strouhal shedding frequency (f_s) for the HFA support ($d = 6.3$mm). The Strouhal number ($St \equiv f_s d/U_e$) is ~0.21 [39] for the Reynolds number range, and spectral peaks are observed at frequencies slightly above f_s. This limited measurements to $f_p < 4.0$Hz$(U_e = 1.3\,$m/s$)$. In addition, the spectra at $3 < f_p < 4$Hz were contaminated from a pump natural frequency at ~3.4 Hz. The root-mean-square velocity (u_{rms}) and TI for each condition are shown in Table 1. Note that the reported u_{rms} is

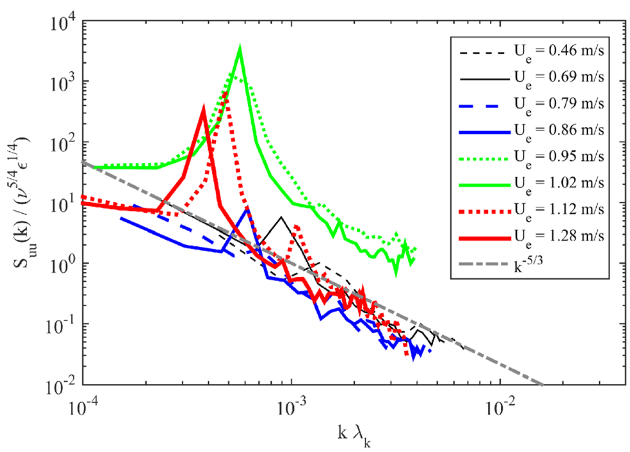

Fig. 3 Test-section inlet power spectra scaled using K41 theory. The dashed line shows the famous $k^{-5/3}$ slope.

Table 1 Summary of unfiltered u_{rms} and the associated turbulence level

f_p (Hz)	1.5	2.0	2.2	2.5	2.7	3.0	3.5	4.0
U_e (m/s)	0.46	0.63	0.69	0.79	0.86	0.95	1.1	1.3
u_{rms} (mm/s)	0.8	2.2	1.2	1.0	1.2	5.1	6.1	5.1
TI (%)	0.16	0.35	0.17	0.13	0.14	0.53	0.55	0.39

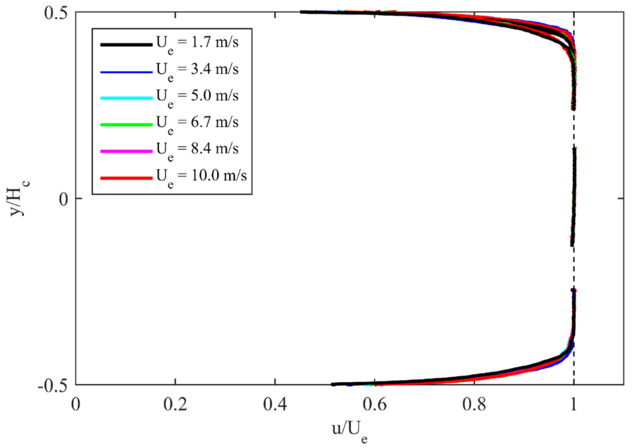

Fig. 4 The mean streamwise velocity (u) from ($x \sim 0.5$m; $z = 0$) scaled with U_e and the test-section height (H_c)

without filtering out the Strouhal or pump natural frequency content. Thus, the mean inlet TI of $\sim$0.30% ($\pm$0.04%) is an upper limit. A bandpass Butterworth filter, with cutoff frequencies of 8 Hz and f_s, reduces the TI to $\sim$0.13%. Note that the freestream TI from PIV was $\sim$1% for all test conditions, which is the PIV uncertainty. This indicates that over the entire operation range, the inlet TI $<$ 1%, which is a common requirement for a low-turbulence facility.

3.3 Mean Velocity Distribution. Scaled mean velocity profiles at $x \sim 0.5$m and $z = 0$ are given in Fig. 4 to quantify the mean shear outside of the developing boundary layer. These profiles are a composite of three independent measurements (top, middle, and bottom). The maximum standard deviation of the three measurements of U_e for any test speed was 1.3% of the mean. This is comparable to the PIV uncertainty, thus there is negligible mean shear outside of the boundary layer. The top boundary layer profiles at $U_e \geq 3.2$m/s are scaled with outer variables in Fig. 5. Lower speeds do not collapse due to pressure-gradient effects, as predicted by the K' criteria. The power-law fit in Fig. 5, $u/U_e = 1.01(y_n/\delta)^{1/7.03}$, supports the design assumption

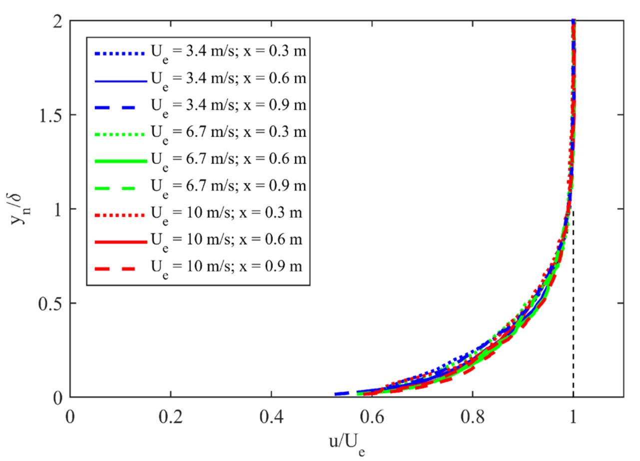

Fig. 5 Outer variable (δ, U_e) scaled mean velocity profiles

Table 2 Measured properties of the boundary layer on the top wall of the test section

x (mm)	U_e (m/s)	Re_x ($\times 10^5$)	δ (mm)	δ* (mm)	θ (mm)	H	u_τ (m/s)	l_ν (μm)
302	1.65	5.0	12.4	1.52	1.14	1.33	NA	NA
555	1.68	9.4	11.7	1.59	1.20	1.32	0.07	14.2
935	1.73	16.2	15.8	1.99	1.53	1.30	0.07	14.2
302	3.30	10.0	9.1	1.17	0.88	1.33	NA	NA
555	3.36	18.6	11.2	1.30	1.00	1.30	0.14	7.4
935	3.46	32.4	16.1	2.04	1.56	1.31	0.14	7.4
302	6.64	20.0	10.6	1.34	1.02	1.32	NA	NA
555	6.73	37.4	11.8	1.27	1.00	1.27	0.26	3.8
935	6.90	64.5	15.9	1.81	1.43	1.26	0.26	3.8
302	10.0	30.1	9.4	1.19	0.91	1.31	NA	NA
555	10.1	56.2	10.7	1.23	0.97	1.27	0.39	2.6
935	10.4	96.8	17.4	1.78	1.42	1.25	0.38	2.6

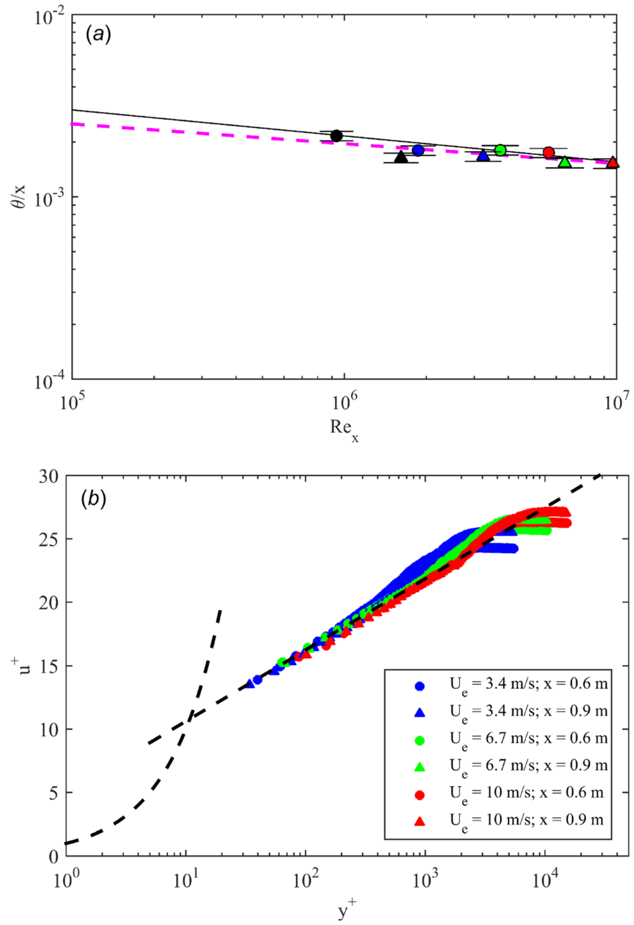

Fig. 6 (a) Scaled momentum thickness versus Reynolds number with the dashed and solid lines being the power-law fit and canonical ZPG flat-plate solution [25], respectively. (b) Inner variable scaled velocity profiles compared to the log-law, $u^+ = \ln(y^+)/0.41+5.0$.

that the velocity profile can be approximated as a 1/7th power-law profile.

The momentum thickness (θ), shape factor, and other boundary layer parameters are provided in Table 2. Beyond $x = 0.3$ m, θ showed excellent collapse (Fig. 6(a)) using traditional Reynolds number scaling, $\theta/x = 0.00878\mathrm{Re}_x^{-0.1086}$. Note that while these scaled results closely follow the canonical curve [25], the boundary layers were thicker (virtual origins were computed to confirm). The curve fit combined with flat-plate momentum integral analysis, $C_f = 2d\theta/dx$, allows an estimate of τ_w, where $C_f(\equiv \tau_w/0.5\rho U_e^2)$ is the coefficient of friction. The resulting inner

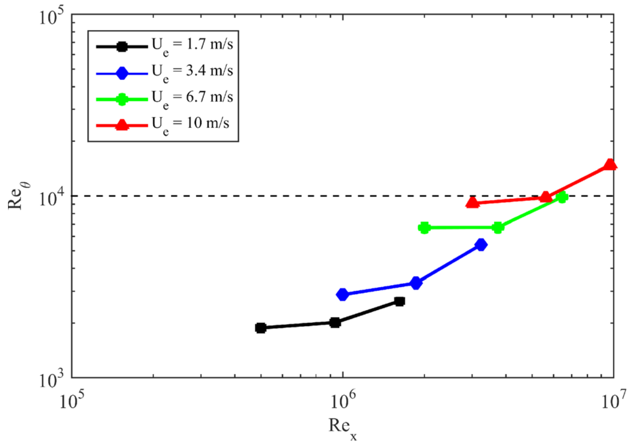

Fig. 7 Re_θ operation range as a function of Re_x for a given free-stream speed

variable scaled profiles are in Fig. 6(*b*). For reference, dashed lines corresponding to the viscous sublayer $(u^+ = y^+)$ and the log-law area included. The measurements do not extend to the viscous sublayer, which is typical of high-Reynolds number TBL measurements. However, there is a significant overlap region that follows the log-law with the higher Reynolds number profiles extending to larger y^+ values. The scatter within the overlap region is due to the limited accuracy of the θ-gradient (<2% change in u_τ collapses the data and the uncertainty of u_τ is ~5%).

4 Conclusions

The current work offers a guide to the overall design of a high-Reynolds number recirculating water tunnel that bridges the gap between commercial water tunnels that are barely turbulent ($Re_\theta \sim 10^3$) and the world's largest facilities ($Re_\theta \sim 10^5$). The design specifications for the current facility were to achieve $Re_\theta \geq 10^4$ (see Fig. 7), maximize test-section optical access, and minimize flow nonuniformity at the test-section inlet. The final design resulted from an iterative process matching pump selection and total system losses. PIV measurements showed the maximum test section speed of 10 m/s, which confirmed the facility design. The inlet flow quality was conditioned with a tandem honeycomb configuration (with settling chambers) sized assuming that the turbulent integral length scale was proportional to the pipe diameter and empirical relationships from the literature [31]. Following the flow straighteners, an 8.5:1 area contraction with a fifth-order polynomial contraction shape reduced TI and increased the flow speed. The overall flow conditioning design was assessed with measurements of the inlet turbulence and mean velocity. Turbulence spectra followed the $k^{-5/3}$ slope for isotropic turbulence and the average TI was <0.3%. Variation in the mean velocity outside of the boundary layer was ~1.3%. The test section was sized using momentum integral analysis for a flat-plate ZPG TBL. The final cross-sectional area $(152\,\mathrm{mm} \times 152\,\mathrm{mm})$ was selected to minimize pressure-gradient effects. The mean boundary layer profiles scaled with outer and inner variables conform to the traditional 1/7th profile and the log-law, respectively. Overall, the test-section wall TBL conform to the classical ZPG TBL (e.g., outer variable scaling, inner variable scaling, and shape factor) over the majority of operating conditions, which confirms the overall facility design.

Acknowledgment

The authors would like to thank Dan Diehl at Diehl Aero-Nautical and Eddie Bryan at Weamco for going above and beyond to ensure that the final product matched the design objectives. In addition, we thank CEAT technical staff (Gary Thacker, Ron Markum, and Gerry Battles) and EFPL students (Dalton Dunlap, Shahrouz Mohagheghian, Jacquelyne Baade, Marcus Lander, Bret Valenzuela, and Shannon Maher) who contributed to the installation, shakedown, and characterization.

Funding Data

- The National Science Foundation (Grant No. 1604978) (Dr. Ronald Joslin, Program Manager).

References

[1] White, C. M., Dubief, Y., and Klewicki, J., 2012, "Re-Examining the Logarithmic Dependence of the Mean Velocity Distribution in Polymer Drag Reduced Wall-Bounded Flow," Phys. Fluids, **24**(2), p. 021701.
[2] Elbing, B. R., Perlin, M., Dowling, D. R., and Ceccio, S. L., 2013, "Modification of the Mean Near-Wall Velocity Profile of a High-Reynolds Number Turbulent Boundary Layer With the Injection of Drag-Reducing Polymer Solutions," Phys. Fluids, **25**(8), p. 085103.
[3] Reich, D. B., Elbing, B. R., Berezin, C. R., and Schmitz, S., 2014, "Water Tunnel Flow Diagnostics of Wake Structures Downstream of a Model Helicopter Rotor Hub," J. Am. Helicopter Soc., **59**(3), p. 032001.
[4] Etter, R. J., Cutbirth, M. J., Ceccio, S. L., Dowling, D. R., and Perlin, M., 2005, "High Reynolds Number Experimentation in the U.S. Navy's William B Morgan Large Cavitation Channel," Meas. Sci. Technol., **16**(9), pp. 1701–1709.
[5] Park, J. T., Cutbirth, J., and Brewer, W. H., 2005, "Experimental Methods for Hydrodynamic Characterization of a Very Large Water Tunnel," ASME J. Fluids Eng., **127**(6), pp. 1210–1214.
[6] Lauchle, G. C., and Gurney, G. B., 1984, "Laminar Boundary-Layer Transition on a Heated Underwater Body," J. Fluid Mech., **144**(1), pp. 79–101.
[7] Marboe, R. C., Weyer, R. M., Jonson, M. L., and Thompson, D. E., 1993, "Hydroacoustic Research Capabilities in the Large Water Tunnel at ARL Penn State," Symposium on Flow Noise Modeling, Measurement, and Control, New Orleans, LA, Nov. 28–Dec. 3, pp. 125–136.
[8] Arndt, R. E. A., Arakeri, V. H., and Higuchi, H., 1991, "Some Observations of Tip Vortex Cavitation," J. Fluid Mech., **229**(1), pp. 269–289.
[9] Shen, X., Ceccio, S. L., and Perlin, M., 2006, "Influence of Bubble Size on Micro-Bubble Drag Reduction," Exp. Fluids, **41**(3), pp. 415–424.
[10] Makiharju, S. A., Elbing, B. R., Wiggins, A., Schinasi, S., Vanden Broeck, J.-M., Perlin, M., Dowling, D. R., and Ceccio, S. L., 2013, "On the Scaling of Air Entrainment From a Ventilated Partial Cavity," J. Fluid Mech., **732**, pp. 47–76.
[11] Oweis, G. F., Choi, J., and Ceccio, S. L., 2004, "Dynamics and Noise Emission of Laser Induced Cavitation Bubbles in a Vortical Flow Field," J. Acoust. Soc. Am., **115**(3), pp. 1049–1058.
[12] Elbing, B. R., Dowling, D. R., Perlin, M., and Ceccio, S. L., 2010, "Diffusion of Drag-Reducing Polymer Solutions Within a Rough-Walled Turbulent Boundary Layer," Phys. Fluids, **22**(4), p. 045102.
[13] Madavan, N. K., Deutsch, S., and Merkle, C. L., 1984, "Reduction of Turbulent Skin Friction by Microbubbles," Phys. Fluids, **27**(2), pp. 356–363.
[14] Deutsch, S., and Castano, J., 1986, "Microbubble Skin Friction Reduction on an Axisymmetric Body," Phys. Fluids, **29**(11), pp. 3590–3597.
[15] Fontaine, A. A., and Deutsch, S., 1992, "The Influence of the Type of Gas on the Reduction of Skin Friction Drag by Microbubble Injection," Exp. Fluids, **13**(2–3), pp. 128–136.
[16] Nedyalkov, I., 2012, "Design of Contraction, Test Section and Diffuser for a High-Speed Water Tunnel," M.S. thesis, Chalmers University of Technology, Gothenburg, Sweden.
[17] Daniel, L., Mohagheghian, S., Dunlap, D., Ruhlman, E., and Elbing, B. R., 2015, "Design of a High Reynolds Number Recirculating Water Tunnel," ASME Paper No. IMECE2015-52030.
[18] Wosnik, M., and Arndt, R. A., 2006, "Testing of a 1:6 Scale Physical Model of the Large, Low-Noise Cavitation Tunnel (LOCAT)," St. Anthony Falls Laboratory, Minneapolis, MN, Project Report No. 486.
[19] Mori, T., Komatsu, Y., Kaneko, H., Sato, R., Izumi, H., Yakushiji, R., and Iyota, M., 2003, "Hydrodynamic Design of the Flow Noise Simulator," ASME Paper No. FEDSM2003-45304.
[20] Wetzel, J. M., and Arndt, R. E. A., 1994, "Hydrodynamic Design Considerations for Hydroacoustic Facilities—Part I: Flow Quality," ASME J. Fluids Eng., **116**(2), pp. 324–331.
[21] Arndt, R. E. A., and Weitendorf, E.-A., 1990, "Hydrodynamic Considerations in the Design of the Hydrodynamics and Cavitation Tunnel (HYKAT) of HSVA," Schiffstechnik, **37**(3), pp. 95–103.
[22] Gindroz, B., and Billet, M. L., 1998, "Influence of the Nuclei on the Cavitation Inception for Different Types of Cavitation on Ship Propellers," ASME J. Fluids Eng., **120**(1), pp. 171–178.
[23] Daniel, L., 2014, "Design and Installation of a High Reynolds Number Recirculating Water Tunnel," M.S. thesis, Oklahoma State University, Stillwater, OK.
[24] Farsiani, Y., and Elbing, B. R., 2016, "Characterization of a Custom-Designed, High-Reynolds Number Water Tunnel," ASME Paper No. FEDSM2016-7866.

[25] White, F. M., 2006, *Viscous Fluid Flow*, 3rd ed., McGraw-Hill, New York, pp. 430–438.
[26] Patel, V. C., 1965, "Calibration of the Preston Tube and Limitations on Its Use in Pressure Gradients," J. Fluid Mech., **23**(1), pp. 185–208.
[27] Nagib, H. M., and Chauhan, K. A., 2008, "Variations of Von Kármán Coefficient in Canonical Flows," Phys. Fluids, **20**(10), p. 101518.
[28] Oweis, G. F., Winkel, E. S., Cutbrith, J. M., Ceccio, S. L., Perlin, M., and Dowling, D. R., 2010, "The Mean Velocity Profile of a Smooth-Flat-Plate Turbulent Boundary Layer at High Reynolds Number," J. Fluid Mech., **665**, pp. 357–381.
[29] Schultz, M. P., 2002, "The Relationship Between Frictional Resistance and Roughness for Surfaces Smoothed by Sanding," ASME J. Fluids Eng., **124**(2), pp. 492–499.
[30] Acharya, M., Bornstein, J., and Escudier, M. P., 1986, "Turbulent Boundary Layers on Rough Surfaces," Exp. Fluids, **4**(1), pp. 33–47.
[31] Lumley, J. L., and McMahon, J. F., 1967, "Reducing Water Tunnel Turbulence by Means of a Honeycomb," ASME J. Basic Eng., **89**(4), pp. 764–770.
[32] Loehrke, R. J., and Nagib, H. M., 1976, "Control of Free-Stream Turbulence by Means of Honeycombs—A Balance Between Suppression and Generation," ASME J. Fluids Eng., **98**(3), pp. 342–355.
[33] Nagib, H. M., Marion, A., and Tan-Atichat, J., 1984, "On the Design of Contractions and Settling Chambers for Optimal Turbulence Manipulation in Wind Tunnels," AIAA Paper No. 84-0536.
[34] Purdy, H. G., 1948, "Model Experiments for the Design of a Sixty Inch Water Tunnel," St. Anthony Falls Laboratory, Minneapolis, MN, Technical Report No. 10.
[35] Morel, T., 1975, "Comprehensive Design of Axisymmetric Wind-Tunnel Contractions," ASME J. Fluids Eng., **97**(2), pp. 225–233.
[36] Bell, J. H., and Mehta, R. D., 1988, "Contraction Design for Small Low-Speed Wind Tunnels," NASA, Mountain View, CA, Report No. NASA-CR-177488.
[37] Hasselmann, K., Reinker, F., au der Wiesche, S., and Kenig, E. Y., 2015, "Numerical Optimization of a Piece-Wise Conical Contraction Zone of a High-Pressure Wind Tunnel," ASME Paper No. AJKFluids2015-15064.
[38] Wetzel, J. M., and Arndt, R. E. A., 1994, "Hydrodynamic Design Considerations for Hydroacoustic Facilities—Part II: Pump Design Factors," ASME J. Fluids Eng., **116**(2), pp. 332–337.
[39] Roshko, A., 1961, "Experiments on the Flow Past a Circular Cylinder at Very High Reynolds Number," J. Fluid Mech., **10**(3), pp. 345–356.